Extension of the rotation-rate measurement range with no sensitivity loss in a cold-atom gyroscope

Yuan Zhao,[1] Xuguang Yue,[2] Fusheng Chen,[1,2] and Chen Huang[2,*]

[1]*Wuhan National Laboratory for Optoelectronics, Huazhong University of Science and Technology, Wuhan 430074, People's Republic of China*

[2]*Huazhong Institute of Electro-Optics, Wuhan National Laboratory for Optoelectronics, Wuhan 430223, People's Republic of China*

(Received 29 January 2021; revised 21 May 2021; accepted 24 June 2021; published 12 July 2021)

A cold-atom gyroscope as an intrinsic high-precision sensor has, however, one inevitable limitation for its dynamic application lying in the vanishing fringe contrast beyond the rotation-rate limit. Here, we realize the measurement beyond the rotation-rate limit via the tip-tilt mirror compensation technique in a three-pulse cold-atom gyroscope. The contrasts of both fringes at an external rotation rate of 15°/s or below are fully recovered to about 35%, nearly the same as that in the static condition. We elucidate theoretically that intact rotation information can still be extracted from the phase output even though the mirror completely counteracts its rotation. Before reaching 50% contrast loss, detailed numerical verification shows a two-orders-of-magnitude extension in the dynamic range for the compensated case compared with that without compensation. Further analysis shows that no reduction of sensitivity up to 60°/s is found for our scheme, whereas other schemes have a trade-off between sensitivity and dynamic range. Whereas other schemes have a trade-off between sensitivity and dynamic range, the simulation shows that no reduction to the sensitivity is found for the measurement beyond the rotation-rate limit in our scheme for up to 60°/s. These features are especially of major relevance in applications such as inertial sensing and navigation.

DOI: 10.1103/PhysRevA.104.013312

I. INTRODUCTION

Light-pulse atom interferometry [1–10] uses atom-photon interaction to split, redirect, and recombine matter waves coherently. This technology has been developed into a powerful tool for precision measurement of inertia parameters, such as acceleration [11–14], the gravity gradient [15–22], and rotation [23–35]. In particular, great progress has been made for the cold-atom gyroscope based on light-pulse interferometry due to its vast application in inertial sensing. Tackmann *et al.* [31] presented a procedure for mutually aligning the beam splitters at the microradian level and achieved a resolution for rotation rates of 6.1×10^{-7} (rad s^{-1})/$\sqrt{\text{Hz}}$ [3.5×10^{-5} (° s^{-1})/$\sqrt{\text{Hz}}$]. Stockton *et al.* [32] realized an absolute geodetic rotation measurement and reached an angle random walk of 8.5×10^{-8} (rad s^{-1})/$\sqrt{\text{Hz}}$ [4.9×10^{-6} (° s^{-1})/$\sqrt{\text{Hz}}$]. An interleaving cold-atom inertial sensor using a four-pulse configuration demonstrated by the research group in Sytèmes de Référence Temps Espace [34,35] reached a stability of 3×10^{-10} rad/s (1.7×10^{-8} °/s). These studies successively pushed the short-term sensitivity as well as the long-term stability of the cold-atom gyroscope to its limit.

In spite of the fast development of the sensitivity and accuracy in the static condition, few works have been done to improve the performance of cold-atom gyroscopes under the dynamic situation. Ambiguous-range identification [36] and contrast recovery beyond the rotation-rate limit [37] are found to be two essential capacities in terms of the highly dynamic measurement. By operating two simultaneous, nearly overlapping interferometers, Yankelev *et al.* [38] extend the unambiguous range of a cold-atom interferometer a thousand-fold without compromising the sensitivity. Yet valid rotation information cannot be acquired from the cold-atom gyroscope beyond the rotation-rate limit regardless of the ambiguous free range. The fringe contrast continuously declines exponentially and eventually vanishes as the rotation rate increases. Reference [37] shows the fringe contrast of a cold-atom gyroscope with interrogation time $T = 4.1$ ms nearly vanishes at a rotation rate of 10°/s along the sensitive axis of the gyroscope. Rapidly declining contrast makes it impossible to accomplish a high-precision measurement due to the quickly deteriorating sensitivity [39]. So far, shortening the interrogation time [11] and velocity-selective detection [40] are the two available schemes to extend the dynamic range. Unfortunately, both of them are at the cost of sensitivity, with one reducing the scale factor and the other reducing the atom number detected. This cost severely limits the performance of a cold-atom gyroscope in its dynamic application.

One remarkable work related to contrast recovery is Ref. [41], where Lan *et al.* suppressed the contrast loss due to the Coriolis force in the gravimeter. They improved the contrast by up to 350% using a tip-tilt mirror to compensate for the Earth's rotation of 2.9×10^{-3} °/s, which is almost negligible in the application of the gyroscope. In order to elevate the accuracy of the gravimeter, the research focuses on the elimination of the rotation-induced bias and contrast loss. However, in the realm of rotation sensing, it is most essential to measure

*Corresponding author: hurricane06@163.com

the external rotation with high precision rather than to suppress the rotation. Furthermore, the useability in a gyroscope, the applicable range, and the effect on the performance of the gyroscope of this technique have yet to be revealed.

In this article, we propose a compensation scheme which recovers the fringe contrast beyond the rotation-rate limit with no sensitivity loss in a three-pulse cold-atom gyroscope. By actively controlling the tip-tilt mirror, we fully retrieve the fringe contrast of a cold-atom gyroscope at a rotation rate of 15°/s along the sensitive axis. The instability of the fringe contrast is 1.2% for a 0°/s–15°/s rotation rate, which shows great robustness under varying external rotation. A detailed analysis based on the detuning evolution of the Raman transition shows the physical mechanism of this compensation scheme. Once the rotation is counteracted by the tip-tilt mirror, three parallel Raman pulses give rise to the fringe contrast recovery. The theoretical derivation explicitly illustrates that the rotation information keeps its integrality as the compensation is applied. According to the numerical simulation of the compensated case, we obtain a two-orders-of-magnitude extension in the dynamic range compared to that of previous atom interferometer sensors [30,31,37] with less than 50% contrast loss. Despite the dynamic range extension, further analysis shows that the gyroscope suffers no sensitivity loss in the measurement beyond the rotation-rate limit. With the assist of the ambiguous-free-range extension [36,38], the rotation measurement as well as the inertial navigation in the moving platform can thus be expected.

This paper is organized as follows. Section II demonstrates the experimental setup of the cold-atom gyroscope. Section III gives the result of the fringe contrast in the rotation experiment with and without compensation. A theoretical analysis of the rotation sensing, the rotation-rate limit, and the contrast recovery under tip-tilt mirror compensation are given in Sec. IV. According to the theoretical result of our compensation technique, we reveal in Sec. V that significant dynamic range extension with no sensitivity loss is achievable. Finally, a conclusion is given in Sec. VI.

II. EXPERIMENTAL SETUP

Our cold-atom gyroscope consists of two symmetric ^{87}Rb interferometers with counterpropagating trajectories, as shown in Fig. 1. The sensor head of our atomic gyroscope lies on a rotation platform. The glass-made vacuum chamber in the sensor head is mainly separated into three parts, two three-dimensional magneto-optical traps with a recapturing technique [37] and one common interference region. The interference region is illuminated by three parallel and evenly spaced Raman beams which are created by a set of polarized beam splitters and corresponding wave plates. The Raman beams are aligned at an angle of 80° with respect to the atomic launch direction. We use a common retroreflector mirror attached to the tip of the two piezoelectric actuators to generate counterpropagating Raman beams for Doppler-sensitive measurement. The actuators are actively controlled by the rotation information from the platform both clockwise and counterclockwise, with one pulling the mirror mount and the other one pushing the mirror mount. Both the launch

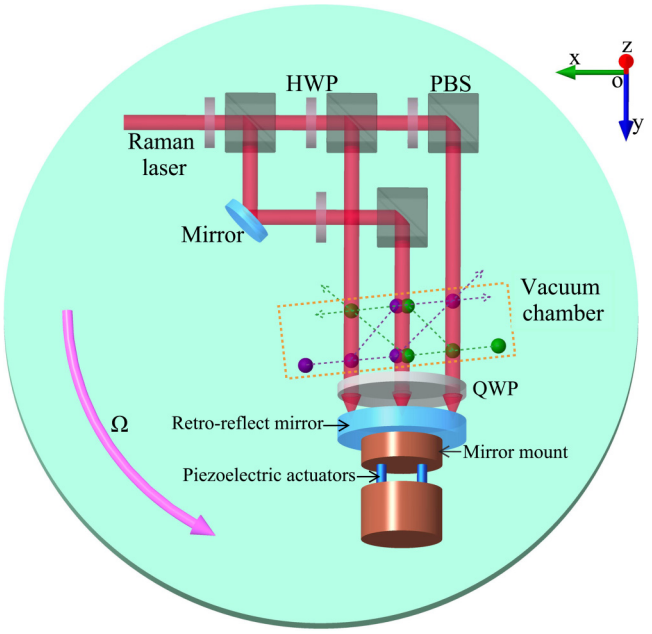

FIG. 1. Sketch of the sensor head and the rotation platform. Our sensor head lies on a rotation platform with rotation rate Ω. The Raman laser is split into three separate Raman beams via a set of half-wave plates (HWP) and polarization beam splitters (PBS). A quarter-wave plate (QWP) is placed on the retroreflector mirror to generate a Raman pulse in the lin⊥lin configuration. The retroreflector mirror is firmly attached to the mirror mount, which is controlled by two piezoelectric actuators (blue). Purple (dark gray) and green (light gray) dashed lines represent the classical trajectories of the two atom clouds [purple (dark grey) and green (light grey) spheres] in the vacuum chamber (orange dashed rectangle) respectively.

directions of the atomic assemblies and the Raman wave vectors are in the horizontal *xoy* plane. As a consequence, the sensitive axis of the cold-atom gyroscope and the rotation axis of the platform are parallel to the z axis.

The experimental sequence of the atom interferometer is as follows. After the 5-ms atomic loading procedure, two atom clouds are launched towards each other at velocities of ±4.4 m/s. The atoms are further cooled down using moving molasses to a temperature of $\mathcal{T} = 30\,\mu$K. The atoms are then prepared in the $|F = 2, m_F = 0\rangle$ state with an efficiency of 90% using optical pumping. An atomic interference sequence consisting of three Raman pulses with durations of 0.6, 1.2, and 0.6 μs with interval $T = 2.825$ ms is applied immediately afterward. Finally, we use a normalized detection technique to obtain the population distribution of the atoms and to suppress the atomic number fluctuation simultaneously. There are two stages in our detection procedure. In the first stage, we detect the fluorescence of the atom in the $|F = 2\rangle$ state. The fluorescence of all the atoms in both $|F = 1\rangle$ and $|F = 2\rangle$ states is gathered in the second stage. Thus, the normalized signals of the two interferometers are [10]

$$P = \frac{N_2}{N_1 + N_2} = \frac{1}{2} + C\cos(\phi_{\rm rot} + \phi_{\rm acc} + \phi_{\rm laser}), \quad (1)$$

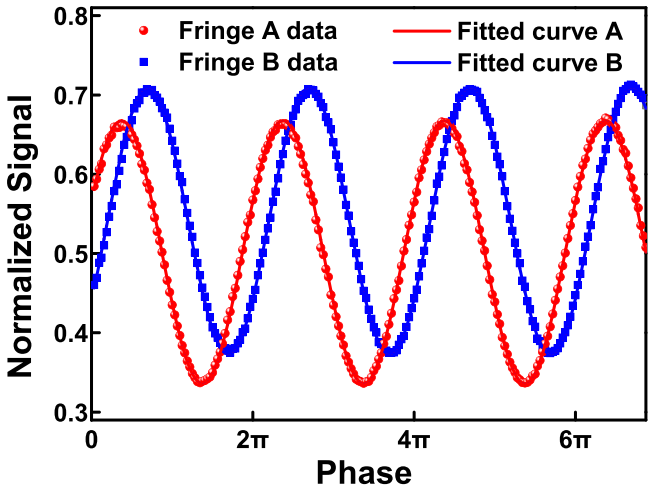

FIG. 2. Two interferometric fringes, A (red dots) and B (blue squares), output under a static environment with a passive vibration-isolation platform. Sine fittings of fringe A [red (light grey) solid line] and fringe B [blue (dark grey) solid line] are also shown.

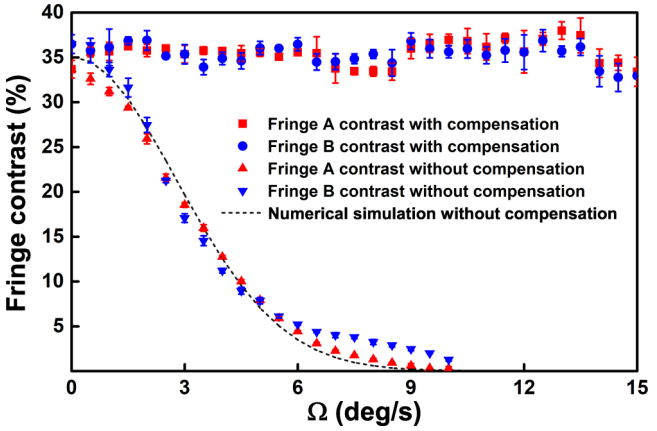

FIG. 3. The fringe contrast versus the rotation rate Ω. The fringe contrasts with tip-tilt mirror compensation for fringe A (red squares) and fringe B (blue dots) show great stability under different rotation rates. The fringe contrasts without compensation for A (red upward triangles) and B (blue downward triangles) decline rapidly as the rotation rate increases, which fits well with the numerical simulation (black dashed line) in Eq. (12).

where $N_{1,2}$ denote the atom number in the $|F = 1, 2\rangle$ states, respectively, C represents the fringe contrast, and the corresponding phases are

$$\begin{aligned} \phi_{\text{rot}} &= -2\mathbf{k}_{\text{eff}} \cdot (\mathbf{v}_L \times \mathbf{\Omega})T^2, \\ \phi_{\text{acc}} &= \mathbf{k}_{\text{eff}} \cdot \mathbf{a}T^2, \\ \phi_{\text{laser}} &= \phi_1 - 2\phi_2 + \phi_3. \end{aligned} \tag{2}$$

Here, $\mathbf{k}_{\text{eff}}$ denotes the effective wave vector of the Raman pulse, $k_{\text{eff}} = |\mathbf{k}_{\text{eff}}| \approx 16 \times 10^6\ \text{m}^{-1}$, $\mathbf{v}_L$ is the longitudinal velocity of each atom which comes from the atomic launch process. $\mathbf{\Omega}$ and $\mathbf{a}$ represent the external rotation and acceleration, respectively, and $\phi_{1,2,3}$ are the phases of three Raman pulses. Thus, rotation and acceleration information can be obtained from these two fringes.

III. CONTRAST RECOVERY BEYOND THE ROTATION-RATE LIMIT

To create a baseline of the fringe contrast, we measured the interferometric fringes in a static environment by scanning the laser phase of the third Raman pulse ϕ_3. Denoting the normalized signals of the two interferometers in the cold-atom gyroscope as A and B, the contrasts of fringes A and B are 33% and 36%, respectively, as shown in Fig. 2. The contrast loss is mainly due to the thermal expansion of the atomic cloud and wave-front distortion.

With the increasing external rotation, the contrasts of both fringes A and B start to decline due to the longitudinal velocity distribution of the atom cloud [37], as illustrated in Fig. 3. The red upward and blue downward triangles represent the fringe contrast versus the rotation rate Ω of fringes A and B, respectively. It is seen that the rotation-rate limit is about 9°/s in our system where the contrasts of both fringes nearly vanish. The contrast under different angular velocities fits well with the theoretical prediction [37], which will be demonstrated and analyzed in Sec. IV B. The fitting result shows the temperature of the atomic clouds is about $\mathcal{T} = 60\,\mu\text{K}$, probably due to optical-pumping-induced heating.

In terms of the fringe contrast with tip-tilt mirror compensation, we actively control the piezoelectric actuator shown in Fig. 1 to counteract the rotation of the platform of each interference cycle completely. We measure five times for each of the rotation rates from 0°/s to 15°/s at intervals of 0.5°/s. Red squares and blue dots represent the mean value of fringes A and B under each rotation rate, respectively. Each error bar denotes the standard deviation of the five measurements for the corresponding rotation rate. As illustrated in Fig. 3, the experimental data show the fringe contrast is fully recovered even if the rotation rate reaches 15°/s. In sharp contrast to the noncompensation scenario, the standard deviation of the fringe contrast is 1.2% from 0°/s to 15°/s, which shows great robustness under varying external rotation.

From the experimental result shown above, we find that using the tip-tilt mirror to compensate the external rotation can retrieve the fringe contrast even for a large rotation rate. We are now interested in the physical mechanism hidden behind and the corresponding effect on the dynamic performance of the gyroscope.

IV. THEORETICAL ANALYSIS OF THE CONTRAST RECOVERY

For a typical three-pulse Mach-Zehnder $\pi/2$-π-$\pi/2$ sequence, the ideal population of the ground state $|a\rangle$ in an atomic interferometer is written as [42]

$$P_a = \tfrac{1}{2}[1 + \cos(\gamma T^2)], \tag{3}$$

where γ is the rate of change of the atom-photon detuning in the Raman transition and we assume that the phases of all three Raman pulses are the same. Here, we notice that the rate of change of the atom-photon detuning is essential to the output phase $\phi_{\text{out}} = \gamma T^2$ for the atomic interferometer. Therefore, in order to explain the mechanism in the tip-tilt

mirror compensation, it is convenient to analyze the evolution of the rate of change of the atom-photon detuning in the external rotation condition first.

A. Physical mechanism for rotation sensing based on the detuning evolution of the Raman transition

For simplicity, let us assume that the Raman beams and the atom launch velocity, both in the horizontal *xoy* plane, are perpendicular to each other. The rotation axis of the rotation platform passes through the retroreflection point of the first Raman pulse and is perpendicular to the horizontal plane. This makes the rotation axis parallel to the sensitive axis of the cold-atom gyroscope. The negligible Earth rotation makes the inertial frame the same as the laboratory frame. As we know, an atomic interferometer senses the average rotation during the whole interference cycle; thus, we consider a counterclockwise rotation Ω which begins at the first Raman pulse and ends at the third Raman pulse. Here, we simplify the wave vector of the Raman pulse $\mathbf{k}_{\text{eff}}$, $\mathbf{v}_L$, and $\mathbf{\Omega}$ to its scalar form k_{eff}, v_L, Ω since we have specified their unit vectors. Under these assumptions, we divide the effect of rotation on the atom-photon interaction into two separate parts as follows.

(i) *Doppler frequency shift due to the atomic velocity projection.* The Doppler frequency shift at the first Raman pulse is zero due to the negligible Raman pulse duration τ. In one interference cycle, the atomic ensemble moves in the inertial space once launched, and the Raman beams rotate with the platform. Thus, at the third Raman pulse, the Raman beams rotate $2\Omega T$, as shown in Fig. 4(a). The velocity of the atomic ensemble now has nonvanishing projection along the Raman beam direction, which leads to the Doppler frequency shift. The frequencies of the Raman beams of the third Raman pulse can be written as

$$\begin{aligned} \omega_1' &= \omega_1 - k_1 v_L \sin(2\Omega T), \\ \omega_2' &= \omega_2 + k_2 v_L \sin(2\Omega T), \end{aligned} \tag{4}$$

where $k_{1,2} = \omega_{1,2}/c$ is the wave number of the two Raman beams with frequencies $\omega_{1,2}$, respectively. The atom-photon detuning at the third Raman pulse is

$$\delta_{R3} = \omega_1' - \omega_2' - \omega_{\text{atom}} = -(k_1 + k_2) v_L \sin(2\Omega T), \tag{5}$$

where $\omega_{\text{atom}} = \omega_b - \omega_a$ is the frequency difference of the two ground states $|a, b\rangle$ with eigenfrequencies $\omega_{a,b}$. In terms of the Doppler frequency shift, the average rate of change of the atom-photon detuning during the whole interference cycle has the form

$$\gamma_1 = \frac{\delta_{R3}}{2T} = -k_{\text{eff}} v_L \Omega, \tag{6}$$

where we use the relation $k_{\text{eff}} = k_1 + k_2$ and the approximation $\sin(2\Omega T) = 2\Omega T$ as $2\Omega T \ll 1$.

(ii) *Phase shift due to the displacement of the retroreflector mirror.* Here, we consider the optical path of two individual Raman beams, k_1 and k_2. Apparently, the retroreflector mirror stays at its original position while the first Raman pulse takes place. The optical paths of k_1 and k_2 are denoted as d_1 and d_2, respectively, as shown in Fig. 4(b). As the platform rotates, the retroreflector mirror and the Raman beams move accordingly. At the third Raman pulse, the optical paths are denoted as d_1' and d_2'. After a few steps of geometry analysis, this displacement leads to the change in the relative optical path of the two Raman beams,

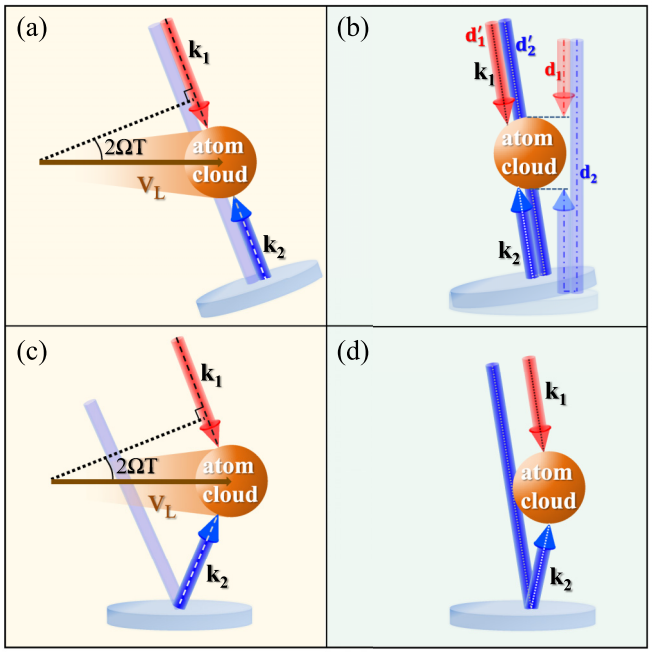

FIG. 4. Sketch of the third Raman pulse with rotation rate Ω and total duration $2T$. (a) The third Raman pulse rotates $2\Omega T$, which leads to the Doppler effect. The frequencies of individual Raman beams k_1 and k_2 are changed correspondingly. (b) The retroreflector mirror rotates and changes the optical path of both k_1 and k_2. The red (light gray) and the blue (dark gray) dash-dotted lines $d_{1,2}$ represent the original optical path of $k_{1,2}$ for the first Raman pulse, respectively. $d_{1,2}'$ represent the optical path of $k_{1,2}$ for the third Raman pulse, respectively. (c) The Doppler frequency shift induced by the projection of the longitudinal velocity of the atoms. Two Raman beams are symmetrically oriented because of the tip-tilt mirror rotates opposite to the rotation platform. (d) The optical paths of $k_{1,2}$ with tip-tilt mirror compensation.

$$\begin{aligned} \phi_{R3} &= k_1(d_1' - d_1) - k_2(d_2' - d_2) \\ &= (k_1 + k_2) 2 v_L T \sin(2\Omega T). \end{aligned} \tag{7}$$

We can transfer the light distance to the rate of change of the detuning as

$$\gamma_2 = \frac{-\phi}{(2T)^2} = -k_{\text{eff}} v_L \Omega. \tag{8}$$

Based on the analysis above, we obtain the total rate of change of the atom-photon detuning as

$$\gamma = \gamma_1 + \gamma_2 = -2k_{\text{eff}} v_L \Omega. \tag{9}$$

It should be noted that Eq. (9) is consistent with the typical expression shown in Eq. (2).

B. Rotation-rate limit in a three-pulse cold-atom gyroscope

One significant limitation in the dynamic application of the cold-atom gyroscopes is the rotation-rate limit [37]. As can be seen from Eqs. (3) and (9), once the velocity of the atoms v_L

is not unified, P_a for each individual atom is different, and therefore, the fringe contrast declines due to the averaging of the phase shift over the longitudinal velocity distribution [43]. Considering the longitudinal velocity distribution due to the atomic temperature, we can rewrite the normalized signal of the gyroscope as

$$P_a = \frac{1}{2} + \int_{-\infty}^{\infty} \cos(2k_{\text{eff}} v_0 \Omega T^2 + 2k_{\text{eff}} v_1 \Omega T^2) g(v_1) dv_1, \tag{10}$$

where we denote $v_L = v_0 + v_1$, v_0 is the center of the velocity distribution of the atomic ensemble along the longitudinal direction, v_1 is the residual velocity fluctuation longitudinally due to the atomic temperature, and $g(v_1)$ is the corresponding Gaussian distribution of v_1,

$$g(v_1) = \sqrt{\frac{m}{2\pi k \mathcal{T}}} e^{-\frac{m v_1^2}{2k\mathcal{T}}}. \tag{11}$$

Here, m represents the atom mass, k is the Boltzmann constant, and $\mathcal{T}$ denotes the temperature of the atomic ensemble. Thus, we can derive the normalized fringe contrast due to the longitudinal velocity distribution as

$$\begin{aligned} C &= \exp\left[-\Omega^2 / \left(2\sigma_\Omega^2\right)\right], \\ \sigma_\Omega &= \frac{1}{2}\sqrt{\frac{m}{k\mathcal{T}}} \frac{1}{k_{\text{eff}} T^2}, \end{aligned} \tag{12}$$

where we assume that the rotation axis is parallel to the sensitive axis of the cold-atom gyroscope. From Eq. (12), we show clearly that the fringe contrast decays exponentially as the rotation rate grows. As we can see from Eq. (10), the longitudinal velocity distribution $g(v_1)$ is coupled to the external rotation Ω. The growing rotation rate gradually amplifies the dephasing phenomenon and eventually washes out the fringe contrast. This is sometimes called the rotation-rate limit [37]. Note that there is no existing criterion for the limitation of the normalized contrast. The actual limitation of the rotation rate Ω_{lim} varies as different criteria are chosen. Here, we are interested in the corresponding dynamic range of the gyroscope. Therefore, it is convenient to use the FWHM as the criterion, in analogy with the laser linewidth. The limitation of the rotation rate is thus

$$\Omega_{\text{lim}}^{\text{FWHM}} = \pm\sqrt{\ln 4}\sigma_\Omega. \tag{13}$$

Under this rotation rate, the normalized contrast is 50%. Also, one can choose e^{-1} to be the boundary for the normalized contrast; the corresponding rotation-rate limit is $\Omega_{\text{lim}}^{1/e} = \pm\sqrt{2}\sigma_\Omega$.

As illustrated in Figs. 5(a) and 5(b), we demonstrate the fringe contrast under different interrogation times and rotation rates for two different atomic temperatures according to the above analytical expression. In Fig. 5(a), the temperature of the atomic ensemble is $\mathcal{T} = 1.5\,\mu\text{K}$, which is nearly the lowest temperature one can achieve without a velocity selection process using ^{87}Rb atoms [44]. Even in this case, the fringe contrast completely vanishes at only $3\,^\circ/\text{s}$ for an interrogation time longer than 10 ms. We note that the majority of Fig. 5(a) is covered in light yellow (light grey), which means the dynamic range and the application scenarios are severely

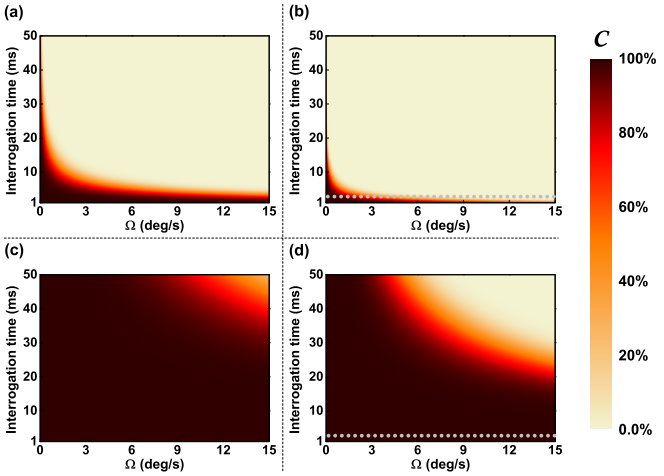

FIG. 5. Numerical simulation of normalized fringe contrast C versus the interrogation time and the external rotation Ω. (a) For $\mathcal{T} = 1.5\,\mu\text{K}$ without compensation. (b) For $\mathcal{T} = 60\,\mu\text{K}$ without compensation. (c) For $\mathcal{T} = 1.5\,\mu\text{K}$ with tip-tilt mirror compensation. (d) For $\mathcal{T} = 60\,\mu\text{K}$ with tip-tilt mirror compensation. The gray dotted lines in (b) and (d) represent the contrast profiles for $T = 2.825$ ms.

limited. As for higher temperature, we show the fringe contrast for $\mathcal{T} = 60\,\mu\text{K}$ in Fig. 5(b). The light yellow (light grey) area is even larger, and the contrast vanishes almost immediately as the gyroscope starts to rotate for $T = 10$ ms. The gray dotted line shows the contrast profile for $T = 2.825$ ms; the fringe contrast vanishes at about $9^\circ/\text{s}$, which is consistent with the black dashed line in Fig. 3. Although the cold-atom gyroscope can reach extremely high precision in measuring Earth's rotation by using a long interrogation time, the above simulation shows that the interrogation time of the gyroscope is severely limited when one measures a relatively large rotation rate. Even if we add an extra velocity-selection process in the atomic preparation procedure, the massive loss in the total atom number leads to significant deterioration in signal-to-noise ratio (SNR), which also has a negative influence on the performance of cold-atom gyroscopes. Therefore, the rotation-rate limit is not fundamental but is a consequence of atom detection protocols averaged over velocity-dependent phase shifts [45]. This usually is an inevitable limit for cold-atom gyroscopes in the Mach-Zehnder configuration.

C. Contrast recovery via tip-tilt mirror compensation

Here, we consider the situation where the retroreflector mirror rotates exactly opposite to the rotation platform. Similar to the analysis above, two parts of the rotation effect are taken into account.

(i) *Doppler frequency shift due to the atomic velocity projection.* As demonstrated in Fig. 4(c), although the individual Raman beam is not perpendicular to the atomic launch direction, the effective wave vectors of all three Raman pulses are perpendicular to the atomic group velocity and perfectly parallel to each other after the tip-tilt mirror compensation is applied. The Doppler frequency shift due to the atomic velocity projection of the third Raman pulse is written as

$$\delta_{R3} = \omega_1' - \omega_2' - \omega_{\text{atom}} = -(k_1 - k_2) v_L \sin(2\Omega T), \tag{14}$$

where

$$\omega_1' = \omega_1 - k_1 v_L \sin(2\Omega T),$$
$$\omega_2' = \omega_2 - k_2 v_L \sin(2\Omega T). \quad (15)$$

(ii) *Phase shift due to the displacement of the retroreflector mirror.* As shown in Fig. 4(d), the piezoelectric actuators counteract the rotation of the retroreflector mirror. Thus, the retroreflect mirror does not rotate with the rotation platform during the interrogation time. Following the same procedure, we can derive the phase shift when the tip-tilt mirror counteracts the rotation as

$$\phi_{R3} = (k_1 - k_2) 2 v_L T \sin(2\Omega T) + \phi_0 \left(1 - \frac{1}{\cos 2\Omega T}\right), \quad (16)$$

where $\phi_0 = k_1 d_1 - k_2 d_2$ is the original accumulated phase difference in the static condition. Following the technique shown above, the total rate of change of the atom-photon detuning γ is

$$\gamma \approx -\frac{\phi_0}{4T^2}\left(1 - \frac{1}{\cos 2\Omega T}\right), \quad (17)$$

where we ignore the terms related to $k_1 - k_2$. After ignoring the high-order terms, we find that the population of the ground state $|a\rangle$ using tip-tilt compensation is

$$P_a = \frac{1}{2}\left[1 + \cos\left(\frac{\phi_0}{2}\Omega^2 T^2\right)\right]. \quad (18)$$

Here, we note that the appearance of the phase term ϕ_0 is the consequence of the optical path change in the individual Raman beam induced by tip-tilt mirror compensation. Counterintuitively, as shown in Eq. (18), the rotation Ω is included in the gyroscope output, although the retroreflector mirror counteracts the rotation entirely. Intact rotation information can still be obtained from only the output phase of the atomic gyroscope as long as the number of periods is identified. More importantly, the atomic group longitudinal velocity v_L vanishes [37]. The decoupling between v_L and external rotation Ω indicates that the stability of the initial velocity no longer affects the scale factor of the gyroscope, which may further improve the long-term stability of the system [46]. We note that here ϕ_0 is a constant in every measuring cycle and does not change with the external rotation rate. Therefore, it can be calibrated by measuring the phase output of the gyroscope under different external rotations, which is similar to the standard procedure for calibrating the scale factor.

From Eq. (18), it seems that the fringe contrast is irrelevant to the external rotation. However, as $d_{1,2}$ is related to its lateral movement along the Raman beam directions for an individual atom, ϕ_0 becomes a function of the lateral velocity $\phi_0(v_r)$. Therefore, the lateral thermal expansion of the atom cloud must be taken into account. The original accumulated phase for an individual atom is

$$\phi_0(v_r) = \phi_0(0) - 2k_{\text{eff}} v_r T, \quad (19)$$

where v_r is the lateral velocity of an individual atom along the Raman beam direction and $\phi_0(0)$ is the original accumulated phase for the atoms with vanishing lateral velocity. In fact, the group velocity for the whole atomic ensemble along the Raman beam direction is zero; therefore, one should use the constant $\phi_0(0)$ in Eq. (18) when considering the overall phase output of the gyroscope. Substituting Eq. (19) into Eq. (17), we can rewrite the rate of change of the atom-photon detuning in Raman transitions as

$$\gamma \approx -\frac{\phi_0(0) - 2k_{\text{eff}} v_r T}{4T^2}\left(1 - \frac{1}{\cos 2\Omega T}\right). \quad (20)$$

Substituting Eq. (20) into Eq. (3) and integrating over the lateral velocity distribution of the atomic cloud, we obtain the output signal with the thermal expansion as

$$P_a = \frac{1}{2} + \int_{-\infty}^{\infty} \cos\left(\frac{\phi_0(0)}{4}\chi - \frac{2k_{\text{eff}} v_r T}{4}\chi\right) g(v_r) dv_r, \quad (21)$$

where $\chi = 1 - \frac{1}{\cos 2\Omega T}$. Thus, we can derive the corresponding normalized fringe contrast as

$$C = \exp\left(-\frac{k_{\text{eff}}^2 \chi^2 k \mathcal{T}_r T^2}{8m}\right), \quad (22)$$

where $\mathcal{T}_r$ denotes the temperature of the atomic cloud along the propagating direction of the first Raman beam. This explicitly shows that the longitudinal velocity distribution is now completely decoupled from the rotation Ω. It is the lateral, rather than longitudinal, temperature that affects the fringe contrast as the external rotation increases.

As depicted in Figs. 5(c) and 5(d), we demonstrate the normalized contrast C with tip-tilt mirror compensation versus the rotation rate Ω and the interrogation time T. In sharp contrast to the uncompensated case in Fig. 5(a), the normalized fringe contrast never drops below 40% in the whole parameter region for $\mathcal{T} = 1.5\,\mu$K, as illustrated in Fig. 5(c). Nearly 100% normalized contrast is achieved at $10^\circ/$s for $T = 50$ ms. Even for the $\mathcal{T} = 60\,\mu$K case, the light yellow (light grey) area is much smaller than that in the uncompensated situation. In agreement with the experimental result, a robust fringe contrast can be achieved in a considerably large region of external rotation. The numerical verification shows that the normalized contrast is nearly fixed at 100% for $T = 2.825$ ms [gray dotted line in Fig. 5(d)]. The fringe contrast hardly decreases for an interrogation time shorter than 10 ms. The light yellow (light grey) areas in the top right corners of Figs. 5(c) and 5(d) indicate that the fringe contrast declines significantly only at large external rotation with a relatively large interrogation time. One notes that, from Eq. (22), extra cooling along the Raman pulse direction can further increase the robustness of the fringe contrast. With the assist of velocity selection using stimulated Raman transition (VSSRT) [47], the lateral temperature can easily be suppressed to less than 1 μK. In this circumstance, the VSSRT can improve both the interaction efficiency of the Raman transition and, more importantly, the robustness of the fringe contrast at the same time. In addition, it can be seen from Figs. 5(c) and 5(d) that there is still a trade-off between large fringe contrast and long interrogation time after the compensation is applied. As for the application of the gyroscopes, one should always concentrate on the accuracy of the whole system. Therefore, by the criterion of good sensitivity, we can derive a set of optimal interrogation times under different external rotations with compensation if we substitute Eq. (22) into Eq. (23).

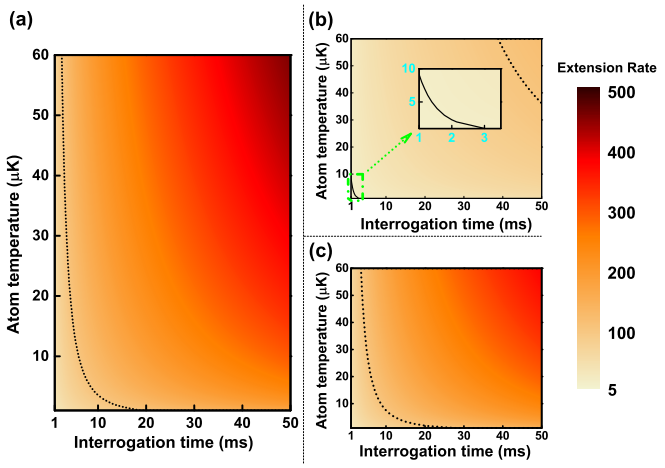

FIG. 6. The extension ratio of the rotation rate before 50% contrast loss is reached via rotation compensation versus the interrogation time T and atom temperature $\mathcal{T}$. (a) The extension ratio of the dynamic range between the tip-tilt mirror compensation and the absence of compensation. (b) The extension ratio of the dynamic range between the tip-tilt mirror compensation and halving the interrogation time. The x axis represents the interrogation time of the tip-tilt mirror compensation scheme. Inset: The black solid line denotes an extension rate larger than 10 to the right. (c) The extension ratio of the dynamic range between the tip-tilt mirror compensation and velocity-sensitive detection. For the velocity-sensitive detection scheme, we extract the phase signal from the atoms within the velocity range $\pm\sqrt{\frac{k\mathcal{T}}{m}}$ of the Gaussian distribution. Extension in the dynamic range greater than two orders of magnitude appears to the right of the black dotted line.

Here, we are interested in not only the contrast recovery but, more importantly, the performance improvement of cold-atom gyroscopes in a highly dynamic situation by using tip-tilt mirror compensation. In order to show the advantages of our scheme more clearly, we give an overall comparison of the dynamic performance of the interferometer between our scheme and others in the next section.

V. DYNAMIC RANGE EXTENSION WITH NO SENSITIVITY LOSS

For high-precision and highly dynamic measurement, the dynamic range and the sensitivity are two essential factors for the atomic gyroscope. Compared to the other two schemes [11,40], two key advantages of our compensation arise and are presented in this section, followed by a discussion for experimental realization.

(i) *A two-orders-of-magnitude extension in the dynamic range is achieved for less than 50% contrast loss.* In order to show the extension of the dynamic range explicitly, we compare the rotation rate of the atomic gyroscope of 50% contrast loss for different interrogation times with and without the tip-tilt mirror compensation, as illustrated in Fig. 6(a). The dynamic range extension represents the ratio of the corresponding external rotation with and without the compensation while the normalized fringe contrast equals 50%. The red region in the top right corner shows that an apparatus with a long interrogation time ($T \geqslant 20$ ms), which is widely used in accuracy-oriented measurements, gains the benefit of the dynamic range extension well above 100 times. As a consequence, the theoretical potential of the high-precision apparatus is extended significantly via this compensation technique.

In comparison to other available compensation techniques, i.e., shortening the interrogation time [11] and velocity-sensitive detection [40], as depicted in Figs. 6(b) and 6(c), it is revealed that our tip-tilt mirror compensation scheme dominates the others in terms of the dynamic range. We show the advantage of a dynamic range almost 10 times or even 100 times greater than the dynamic range from halving the interrogation time and for velocity-sensitive detection schemes. As illustrated in Fig. 6(b), the black solid line is located in the bottom left corner, which means a dynamic range extension of 10 times or more is almost guaranteed for all parameter regions shown. Especially, a two-orders-of-magnitude extension appears for a long interrogation time and high atom temperature. Counterintuitive to common sense, for choosing atoms within the velocity range of $\pm\sqrt{\frac{k\mathcal{T}}{m}}$, the velocity-sensitive detection scheme shows little improvement in terms of the dynamic range, as illustrated in Fig. 6(c). An extension in dynamic range for tip-tilt mirror compensation 100 times or more larger than the velocity-selected detection scheme can be achieved to the right of the black dotted line.

(ii) *No sensitivity loss occurs for measurement beyond the rotation-rate limit.* The sensitivity of the cold-atom interferometer relies on various kinds of parameters, which is written as [39]

$$\text{Sensitivity} = \frac{1}{C}\frac{1}{R_{\text{SN}}}\frac{1}{k_{\text{eff}} v_L T^2}, \tag{23}$$

where R_{SN} denotes the signal-to-noise ratio. Usually, the effective wave number k_{eff}, the atomic launch velocity v_L, and the interrogation time T have negligible fluctuations during successive measurement periods. Despite the current-related noise, the signal-to-noise ratio largely depends on the atom number detected, which is also relatively stable. Meanwhile, the fringe contrast C, as shown in Fig. 3, is sensitive to the external rotation. Without any compensation, apparently, the sensitivity continuously deteriorates with increasing rotation rate due to the rapidly decrease fringe contrast. One intuitive solution for increasing the dynamic range is to decrease the interrogation time. By choosing a shorter interrogation time T_s, the sensitivity is reduced by the ratio of $(T/T_s)^2$ compared to the static measurement even if we neglect the remaining contrast loss due to the longitudinal velocity distribution. The other solution is to use velocity-sensitive detection, which uses a nonperpendicular detection beam to detect the fluorescence of the atoms with a certain Doppler frequency shift. Although this technique reduces the longitudinal velocity distribution of the detected atoms and recovers the fringe contrast, the selection significantly reduces the total number of atoms detected. The narrower the velocity distribution one selects, the more atoms one abandons, and the worse the SNR is. Thus, we cannot realize a highly dynamic measurement without sensitivity loss via these two schemes.

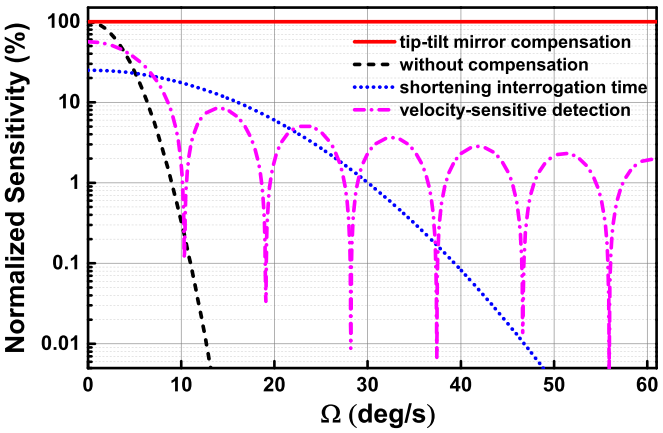

FIG. 7. The normalized sensitivity of the interferometer with $T = 2.825\,\text{ms}$ and atomic temperature $\mathcal{T} = 60\,\mu\text{K}$ versus the external rotation for tip-tilt mirror compensation (red solid line), no compensation (black dashed line), halving the interrogation time (blue dotted line), and velocity-sensitive detection (pink dash-dotted line). The velocity width of the velocity-sensitive detection is the same as that in Fig. 6. In order to present the decay of the sensitivity explicitly, we here use a logarithmic axis for the normalized sensitivity.

On the other hand, in our scheme, the interrogation time and the atom number detected are the same as those in static environment. Therefore, no compromise of the sensitivity has to be made to achieve the measurement capability beyond the rotation-rate limit. As shown in Fig. 7, we evaluate the sensitivity of the interferometer as the external rotation increases using the normalized sensitivity as

$$\text{Normalized sensitivity} = \frac{S_{\text{ori}}}{S_{\text{rot}}} \times 100\%, \tag{24}$$

where S_{ori} represents the initial sensitivity of the interferometer in the static condition and S_{rot} represents the sensitivity of the interferometer under different rotation rates Ω for four different cases. The logarithmic axis shows clearly that the sensitivity in the no-compensation case deteriorates rapidly as the external rotation increases. If we decrease the interrogation time to half of its original duration, the measurement beyond the initial rotation-rate limit can be obtained; however, the maximum normalized sensitivity is merely 25%. Like in the previous situation, by utilizing velocity-sensitive detection, the signal-to-noise ratio decreases due to a 32% loss of the total atom number as we choose atoms within the velocity range of $\pm\sqrt{\frac{k\mathcal{T}}{m}}$ of the Gaussian distribution, and thus, the sensitivity decreases correspondingly. In fact, the periodically deteriorating sensitivity makes it impossible for high-precision, highly dynamic rotation sensing. In sharp contrast, no visible sensitivity loss occurs even for external rotation up to $60^\circ/\text{s}$ using tip-tilt mirror compensation.

In experimental realization, the dynamic range and sensitivity may further deteriorate. In terms of the dynamic range, the extension is mainly limited by the travel range of the piezoelectric actuator. In order to compensate the external rotation completely, the retroreflector mirror needs to rotate $\theta_{\text{mir}} = 2\Omega T$ within a time of $2T$. A commercial closed-loop piezoelectric actuator nowadays can induce a rotation of roughly $\pm 1.15^\circ$ at its maximum. Thus, the dynamic range is limited to $170^\circ/\text{s}$ for $T = 2.852\,\text{ms}$ or $11.5^\circ/\text{s}$ for $T = 50\,\text{ms}$. In terms of the sensitivity loss, controlling the tip-tilt mirror can certainly induce vibration noise and rotation noise, both of which can reduce the sensitivity. Through the accelerometer mounted behind the retroreflector mirror, one can measure the acceleration of the mirror and suppress the vibration noise from the signal output [48,49]. In addition, the rotation noise can be reduced by using piezoelectric actuators with voltage feedback control.

VI. CONCLUSIONS

In conclusion, we investigated a tip-tilt mirror compensation scheme in a three-pulse cold-atom gyroscope in detail, which could be used in high-precision, highly dynamic rotation measurements. By using the tip-tilt mirror to counteract the external rotation, we fully recover the fringe contrast of the three-pulse cold-atom gyroscope to that in the static condition (35%) at $0^\circ/\text{s}$–$15^\circ/\text{s}$. The fringe contrast with a standard deviation of 1.2% shows excellent robustness against different rotation rates and dramatically increases the dynamic performance of the atomic gyroscope. The population of the atoms embodies the intact external rotation information instead of the residual even though the compensation is applied. In particular, with the three parallel Raman pulses, the longitudinal velocity and its distribution are decoupled from the external rotation, which may further improve the long-term stability of the gyroscope. Numerical verification of the fringe contrast and dynamic range revealed that this compensation scheme can extend the dynamic range by two orders of magnitude. More importantly, the sensitivity of the system remains unchanged from the static condition to a rotation rate up to $60^\circ/\text{s}$. Such a highly dynamic range, high-precision cold-atom gyroscope offers a promising alternative for the next generation of high-performance inertial navigation systems.

ACKNOWLEDGMENTS

We thank H. Yao and X. Song for their contributions to the apparatus, T. Lv and G. Luan for collaboration in the laboratory, and J. Cheng and H. Song for stimulating discussions. X.Y. acknowledges support from the National Natural Science Foundation of China (Grant No. 11504328).

[1] M. A. Kasevich and S. Chu, Atomic Interferometry Using Stimulated Raman Transitions, Phys. Rev. Lett. **67**, 181 (1991).

[2] F. Riehle, T. Kisters, A. Witte, J. Helmcke, and C. J. Bordé, Optical Ramsey Spectroscopy in a Rotating Frame: Sagnac Effect in a Matter-Wave Interferometer, Phys. Rev. Lett. **67**, 177 (1991).

[3] D. W. Keith, C. R. Ekstrom, Q. A. Turchette, and D. E. Pritchard, An Interferometer for Atoms, Phys. Rev. Lett. **66**, 2693 (1991).

[4] O. Carnal and J. Mlynek, Young's Double-Slit Experiment with Atoms: A Simple Atom Interferometer, Phys. Rev. Lett. **66**, 2689 (1991).

[5] A. D. Cronin, J. Schmiedmayer, and D. E. Pritchard, Optics and interferometry with atoms and molecules, Rev. Mod. Phys. **81**, 1051 (2009).

[6] B. Barrett, R. Geiger, I. Dutta, M. Meunier, B. Canuel, A. Gauguet, P. Bouyer, and A. Landragin, The Sagnac effect: 20 years of development in matter-wave interferometry/L'effet Sagnac: 20 ans de développements des interféromètres à ondes de matière, C. R. Phys. **15**, 875 (2014).

[7] B. Barrett, A. Bertoldi, and P. Bouyer, Inertial quantum sensors using light and matter, Phys. Scr. **91**, 053006 (2016).

[8] K. Bongs, M. Holynski, J. Vovrosh, P. Bouyer, G. Condon, E. Rasel, C. Schubert, W. P. Schleich, and A. Roura, Taking atom interferometric quantum sensors from the laboratory to real-world applications, Nat. Rev. Phys. **1**, 731 (2019).

[9] M. S. Safronova, D. Budker, D. DeMille, D. F. Jackson Kimball, A. Derevianko, and C. W. Clark, Search for new physics with atoms and molecules, Rev. Mod. Phys. **90**, 025008 (2018).

[10] P. R. Berman, *Atom Interferometry* (Academic, San Diego, 1997).

[11] Y. Bidel, N. Zahzam, C. Blanchard, A. Bonnin, M. Cadoret, A. Bresson, D. Rouxel, and M. F. Lequentrec-Lalancette, Absolute marine gravimetry with matter-wave interferometry, Nat. Commun. **9**, 627 (2018).

[12] V. Ménoret, P. Vermeulen, N. L. Moigne, S. Bonvalot, P. Bouyer, A. Landragin, and B. Desruelle, Gravity measurements below 10^{-9} g with a transportable absolute quantum gravimeter, Sci. Rep. **8**, 12300 (2018).

[13] R. Caldani, K. X. Weng, S. Merlet, and F. Pereira Dos Santos, Simultaneous accurate determination of both gravity and its vertical gradient, Phys. Rev. A **99**, 033601 (2019).

[14] G. Stern, B. Battelier, R. Geiger, G. Varoquaux, A. Villing, F. Moron, O. Carraz, N. Zahzam, Y. Bidel, W. Chaibi, F. P. Dos Santos, A. Bresson, A. Landragin, and P. Bouyer, Light-pulse atom interferometry in microgravity, Eur. Phys. J. D **53**, 353 (2009).

[15] J. M. McGuirk, G. T. Foster, J. B. Fixler, M. J. Snadden, and M. A. Kasevich, Sensitive absolute-gravity gradiometry using atom interferometry, Phys. Rev. A **65**, 033608 (2002).

[16] N. Yu, J. M. Kohel, J. R. Kellogg, and L. Maleki, Development of an atom-interferometer gravity gradiometer for gravity measurement from space, Appl. Phys. B **84**, 647 (2006).

[17] F. Sorrentino, Q. Bodart, L. Cacciapuoti, Y.-H. Lien, M. Prevedelli, G. Rosi, L. Salvi, and G. M. Tino, Sensitivity limits of a Raman atom interferometer as a gravity gradiometer, Phys. Rev. A **89**, 023607 (2014).

[18] G. W. Biedermann, X. Wu, L. Deslauriers, S. Roy, C. Mahadeswaraswamy, and M. A. Kasevich, Testing gravity with cold-atom interferometers, Phys. Rev. A **91**, 033629 (2015).

[19] I. Perrin, Y. Bidel, N. Zahzam, C. Blanchard, A. Bresson, and M. Cadoret, Proof-of-principle demonstration of vertical-gravity-gradient measurement using a single-proof-mass double-loop atom interferometer, Phys. Rev. A **99**, 013601 (2019).

[20] O. Carraz, C. Siemes, L. Massotti, R. Haagmans, and P. Silvestrin, A spaceborne gravity gradiometer concept based on cold atom interferometers for measuring Earth's gravity field, Microgravity Sci. Technol. **26**, 139 (2014).

[21] G. Rosi, L. Cacciapuoti, F. Sorrentino, M. Menchetti, M. Prevedelli, and G. M. Tino, Measurement of the Gravity-Field Curvature by Atom Interferometry, Phys. Rev. Lett. **114**, 013001 (2015).

[22] S. W. Chiow, J. Williams, and N. Yu, Noise reduction in differential phase extraction of dual atom interferometers using an active servo loop, Phys. Rev. A **93**, 013602 (2016).

[23] J. Fils, F. Leduc, P. Bouyer, D. Holleville, N. Dimarcq, A. Clairon, and A. Landragin, Influence of optical aberrations in an atomic gyroscope, Eur. Phys. J. D **36**, 257 (2005).

[24] B. Canuel, F. Leduc, D. Holleville, A. Gauguet, J. Fils, A. Virdis, A. Clairon, N. Dimarcq, C. J. Bordé, A. Landragin, and P. Bouyer, Six-Axis Inertial Sensor Using Cold-Atom Interferometry, Phys. Rev. Lett. **97**, 010402 (2006).

[25] A. Gauguet, T. E. Mehlstäubler, T. Lévèque, J. Le Gouët, W. Chaibi, B. Canuel, A. Clairon, F. Pereira Dos Santos, and A. Landragin, Off-resonant Raman transitions impact in an atom interferometer, Phys. Rev. A **78**, 043615 (2008).

[26] K. Takase, Precision rotation rate measurements with a mobile atom interferometer, Ph.D. thesis, Stanford University, 2008.

[27] T. Müller, M. Gilowski, M. Zaiser, P. Berg, C. Schubert, T. Wendrich, W. Ertmer, and E. M. Rasel, A compact dual atom interferometer gyroscope based on laser-cooled rubidium, Eur. Phys. J. D **53**, 273 (2009).

[28] G. Tackmann, P. Berg, C. Schubert, S. Abend, M. Gilowski, W. Ertmer, and E. M. Rasel, Self-alignment of a compact large-area atomic Sagnac interferometer, New J. Phys. **14**, 015002 (2012).

[29] P. Berg, S. Abend, G. Tackmann, C. Schubert, E. Giese, W. P. Schleich, F. A. Narducci, W. Ertmer, and E. M. Rasel, Composite-Light-Pulse Technique for High-Precision Atom Interferometry, Phys. Rev. Lett. **114**, 063002 (2015).

[30] Z. W. Yao, S. B. Lu, R. B. Li, J. Luo, J. Wang, and M. S. Zhan, Calibration of atomic trajectories in a large-area dual-atom-interferometer gyroscope, Phys. Rev. A **97**, 013620 (2018).

[31] G. Tackmann, P. Berg, S. Abend, C. Schubert, W. Ertmer, and E. M. Rasel, Large-area Sagnac atom interferometer with robust phase read out, C. R. Phys. **15**, 884 (2014).

[32] J. K. Stockton, K. Takase, and M. A. Kasevich, Absolute Geodetic Rotation Measurement Using Atom Interferometry, Phys. Rev. Lett. **107**, 133001 (2011).

[33] G. W. Biedermann, X. Wu, L. Deslauriers, K. Takase, and M. A. Kasevich, Low-noise simultaneous fluorescence detection of two atomic states, Opt. Lett. **34**, 347 (2009).

[34] D. Savoie, M. Altorio, B. Fang, L. A. Sidorenkov, R. Geiger, and A. Landragin, Interleaved atom interferometry for high sensitivity inertial measurements, Sci. Adv. **4**, eaau7948 (2018).

[35] I. Dutta, D. Savoie, B. Fang, B. Venon, C. L. Garrido Alzar, R. Geiger, and A. Landragin, Continuous Cold-Atom Inertial Sensor with 1 nrad/sec Rotation Stability, Phys. Rev. Lett. **116**, 183003 (2016).

[36] C. Avinadav, D. Yankelev, O. Firstenberg, and N. Davidson, Rotation Sensing with Improved Stability using Point Source Atom Interferometry, Phys. Rev. Appl. **13**, 054053 (2020).

[37] A. V. Rakholia, High data-rate atom interferometry for measuring dynamic inertial conditions, Ph.D. thesis, University of New Mexico, 2015.

[38] D. Yankelev, C. Avinadav, N. Davidson, and O. Firstenberg, Atom interferometry with thousand-fold increase in dynamic range, Sci. Adv. **6**, eabd0650 (2020).

[39] A. Peters, K. Y. Chung, and S. Chu, High-precision gravity measurements using atom interferometry, Metrologia **38**, 25 (2001).

[40] A. Cingoz, M. Zhu, M. Y. Shverdin, and M. Cashen, Velocity selective thermal atomic beam inertial sensor, US Patent No. US10288428 B1 (2019).

[41] S. Y. Lan, P. C. Kuan, B. Estey, P. Haslinger, and H. Müller, Influence of the Coriolis Force in Atom Interferometry, Phys. Rev. Lett. **108**, 090402 (2012).

[42] M. O. Scully and M. S. Zubairy, *Quantum Optics* (Cambridge University, Cambridge, 1997).

[43] T. L. Gustavson, P. Bouyer, and M. A. Kasevich, Precision Rotation Measurement with an Atom Interferometer Gyroscope, Phys. Rev. Lett. **78**, 2046 (1997).

[44] B. Wang, D. S. Lv, Q. Z. Qu, J. B. Zhao, T. Li, L. Liu, and Y. Z. Wang, Laser cooling of ^{87}Rb to 1.5 μK in a fountain clock, Chin. Phys. Lett. **28**, 063701 (2011).

[45] S. M. Dickerson, J. M. Hogan, A. Sugarbaker, D. M. S. Johnson, and M. A. Kasevich, Multiaxis Inertial Sensing with Long-Time Point Source Atom Interferometry, Phys. Rev. Lett. **111**, 083001 (2013).

[46] T. Müller, T. Wendrich, M. Gilowski, C. Jentsch, E. M. Rasel, and W. Ertmer, Versatile compact atomic source for high-resolution dual atom interferometry, Phys. Rev. A **76**, 063611 (2007).

[47] M. Kasevich, D. S. Weiss, E. Riis, K. Moler, S. Kasapi, and S. Chu, Atomic Velocity Selection Using Stimulated Raman Transitions, Phys. Rev. Lett. **66**, 2297 (1991).

[48] S. Merlet, J. Le Gouët, Q. Bodart, A. Clairon, A. Landragin, F. P. Dos Santos, and P. Rouchon, Operating an atom interferometer beyond its linear range, Metrologia **46**, 87 (2009).

[49] J. Lautier, L. Volodimer, T. Hardin, S. Merlet, M. Lours, F. P. Dos Santos, and A. Landragin, Hybridizing matter-wave and classical accelerometers, Appl. Phys. Lett. **105**, 144102 (2014).